Computationally Driven Discovery of Layered Quinary Oxychalcogenides: Potential *p*-Type Transparent Conductors?

Benjamin A. D. Williamson

Department of Chemistry, University College London, 20 Gordon Street, London WC1H 0AJ, UK

Thomas Young Centre, University College London, Gower Street, London WC1E 6BT, United Kingdom

Gregory J. Limburn

Department of Chemistry, University of Southampton, Southampton, SO17 1BJ, UK

Graeme W. Watson

School of Chemistry and CRANN, Trinity College Dublin, The University of Dublin, College Green, Dublin 2, Ireland

Geoffrey Hyett

Department of Chemistry, University of Southampton, Southampton, SO17 1BJ, UK

David O. Scanlon

Department of Chemistry, University College London, 20 Gordon Street, London WC1H 0AJ, UK

Thomas Young Centre, University College London, Gower Street, London WC1E 6BT, United Kingdom

Diamond Light Source Ltd., Diamond House, Harwell Science and Innovation Campus, Didcot, Oxfordshire OX11 0DE, UK

Summary

n-type Transparent conductors (TCs) are key materials in the modern optoelectronics industry. Despite years of research, the development of a high performance *p*-type TC has lagged far behind that of its *n*-type counterparts delaying the advent of "transparent electronics" based on fully transparent p-n junctions. Here, we propose the layered oxysulfide $[Cu_2S_2][Sr_3Sc_2O_5]$ as a structural mo-

Email address: d.scanlon@ucl.ac.uk (David O. Scanlon)

tif for discovering novel *p*-type TCs. We have used density functional theory to screen the thermodynamic and dynamical stability and electronic structure of 24 compositions based on this motif, predicting 2 *p*-type TCs and 8 other stable systems with semiconductor properties. Following our predictions, we have successfully synthesized our best candidate *p*-type TC, $[Cu_2S_2][Ba_3Sc_2O_5]$, which displays structural and optical properties that validate our computational models. It is expected that the design principles emanating from this analysis will move the field closer to the realization of a high figure-of-merit *p*-type TC.

1. Introduction

Transparent conductors (TCs) are ubiquitous in modern life with applications ranging from portable electronics, to gas sensing and photovoltaics.[1] At present the field is dominated by high-mobility, high-conductivity *n*-type materials such as the binary metal oxides: In_2O_3[2,3], SnO_2[4–7], ZnO[8,9], and $BaSnO_3$,[10,11] whilst equivalent *p*-type materials are scarce despite decades of dedicated research.[12–15] The unbalanced nature of this field means that TCs are limited to playing the role of transparent electrodes. Should a high-performance *p*-type TC be found, the fabrication of transparent p-n junctions would bring about the realisation of transparent electronics as well as provide a wider range of materials for use as electrodes in current devices such as photovoltaics.[12,13,16–18]

Multiple design strategies have been created to formulate *p*-type conductivity whilst retaining a large optical band gap to avoid the absorption of visible light ($E_g^{opt} > 3.1$ eV). In particular these are: (i) *p*-type doping of *n*-type TCs[15,19–27], (ii) *(n-1)*$d^{10}ns^2$ metal oxides incorporating main group cations such as Sn^{2+}, Pb^{2+} and Bi^{3+},(iii) spinel oxides such as $ZnCo_2O_4$[28,29] and (iv) the "chemical modulation of the valence band" (CMVB) formulated by Hosono and coworkers in Cu-based oxides.[30]

Details of these methods are described at length by Zhang et al. in ref. [1], but to date the most robust and successful method for designing *p*-type TCs is arguably the CMVB method. Hosono reported that the delafossite $CuAlO_2$ possessed the Cu *3d* – O *2p* mixing present in the valence band of Cu_2O whilst retaining the wider band gap of Al_2O_3.[30] From this study they established design rules that involved the preferential mixing of a d^{10} closed shell cation such as Cu^{1+} with O 2*p* states at the VBM. The effect of this hybridisation is that the typically polaronic nature of holes at the VBM are delocalised lowering the ionisation potential and promoting favourable dispersion. This is also achieved via tetrahedral coordination of oxygen by reducing the non-bonding states by

distributing the electrons along the four σ-bonds[31]. To maintain high optical transparency, the metal cation must be closed shell (d^{10}) in order to avoid intra-atomic excitations (colouration) and the Cu–Cu distances must be significantly high enough in order to avoid direct interactions between the d^{10} electrons neighbouring each Cu ion.

Alongside $CuAlO_2$ other delafossite materials such as $CuGaO_2$[32–35], $CuInO_2$[32,35], $CuCrO_2$[36], $CuBO_2$[34,37,38], $CuScO_2$[32,35,39] and $SrCu_2O_2$[40,41] were studied where in each case, despite being transparent, the *p*-type conductivities were typically several orders of magnitude lower than *n*-type TCs. Acceptor defects in these materials have been shown to be deep in nature and as such degenerate conductivity is not realisable in these materials.[42,43] To date the highest reported conductivity for a delafossite TC is for Mg-doped $CuCrO_2$ ($CuCrO_2$:Mg) of 220 S cm^{-1}.[36]

A natural progression is to extend to the other chalcogenides: S and Se. It has been shown that the band gap decreases from Cu_2O to Cu_2S to Cu_2Se yet with an increase in conductivity.[44–46] This is indicative of more dispersive VBMs at lower ionisation potentials and thus a greater possibility of *p*-type degeneracy. Two layered oxychalcogenides have been shown to have the 50:50 Ch *3d* – Ch *2p* mixing at the VBM whilst retaining wide band gaps, LaCuOS and LaCuOSe. As expected, LaCuOSe (when acceptor doped with Mg) displays higher *p*-type conductivities of 910S cm^{-1} whereas LaCuOS (doped with Sr) possesses conductivities of 2.6×10^{-1}S cm^{-1}.[47,48] The increased hybridisation of Cu *3d* with Se *4p* over S *3p* is the reasoning behind the increased conductivity, however LaCuOSe has a band gap of $\sim$ 2.8 eV whilst LaCuOS is transparent with a band gap of $\sim$ 3.1 eV.[17,49]

Possibly the most promising transparent *p*-type conductor in recent years is the layered oxychalcogenide: $[Cu_2S_2][Sr_3Sc_2O_5]$ which comprises of alternating $[Cu_2S_2]^{2-}$ layers and perovskite-like $[Sr_3Sc_2O_5]^{2+}$ layers and possesses a 3.1 eV band gap. Figure 1 shows the layered $[Cu_2S_2][Sr_3Sc_2O_5]$ structure where the coordination in the copper sulfide layer consists of tetrahedrally bonded Cu ions (with S) in which the S ions are possess a square-based pyramidal configuration to Cu. Within the $[A_3M_2O_5]^{2+}$ layer, there exists square-based pyramids of M^{3+} and O, which in turn are bonded between two M^{3+} cations and within a square planar motif with adjacent A^{2+} ions. The A^{2+} cations are generally coordinated in a square anti-prismatic configuration either with 8 oxygens or 4 oxygens and 4 sulphurs. It was first synthesised by Otzschi and coworkers in 1999[50] and subsequently reinvestigated by Liu et al. in 2007.[51] The latter group displayed *undoped* *p*-type conductivities of 2.8 S cm^{-1} and extremely high hole mobilities of 150 cm^2 V^{-1} s^{-1} despite relatively low carrier concentrations of 10^{17} cm^{-3} suggesting a desirable electronic structure and low formation

energy acceptors.[51] Further to this, hybrid DFT calculations were carried out on $[Cu_2S_2][Sr_3Sc_2O_5]$[37] whereby the electronic structure of the VBM was confirmed to be made up of $\sim$50:50 Cu 3*d* and S 3*p* and the large band gap brought about by the perovskite-like layer.

Using the $[Cu_2S_2][Sr_3Sc_2O_5]$ structure as a prototype allows for a large configurational space of *p*-type transparent conducting materials and thus a greater potential for success in finding low hole effective mass, degenerately dopable materials. This method of computationally driven design has been successfully implemented in advancing the search for new high-mobility transparent *p*-type semiconductors in previous studies.[52–54] Combining this with technological breakthroughs in thin film and solid state synthesis procedures allow for the fabrication of "designer" layered compounds and thus greater control is achievable allowing previously unobtainable metastable or hard-to-synthesise layered compounds to be realised.[55–58] In this work, using cation substitution in the oxide layer we computationally predict 8 layered oxysulfides with optical band gaps spanning the range 0.78 eV to 3.24 eV. Based on our predicted properties, our proposed champion transparent conductor $[Cu_2S_2][Ba_3Sc_2O_5]$ is successfully synthesised, showing excellent agreement with our calculated structural and optical properties.

2. Computational Results

2.1. Thermodynamic Stability Screening

The calculations in this work involved forming variations of the $[Cu_2S_2][A_3M_2O_5]$ structure (tetragonal, *I4/mmm*) where A=**Sr**,Ca,Ba,Mg and M=**Sc**,Al,Ga,In,Y,La. This resulted in 24 compounds with the same stoichiometry as $[Cu_2S_2][Sr_3Sc_2O_5]$ and are named using the convention "AB" eg. $[Cu_2S_2][Sr_3Sc_2O_5]$ is "SrSc" and $[Cu_2S_2][Ba_3Al_2O_5]$ is "BaAl". The thermodynamic stability of the 24 compounds at 0K was calculated relative to $\sim$313 (geometry relaxed) competing stable phases taken from the Inorganic Crystal Structures Database (ICSD).[59] A stability criterion was established from the energy above the convex hull and ranges from 0–0.07 eV atom^{-1} following work by Ceder and coworkers.[60] An absolute maximum can also be applied based upon the synthesis temperature (k_BT, where T = $\sim$800°C) in reference [51] which gives an E above Hull of $\sim$0.09 eV atom^{-1}. Out of the 24 compounds calculated, 9 compounds were identified within this stability criterion. The energies above the convex hull are tabulated in SI Table S4 and those within the stability window are shown in Figure 2. Using this analysis, SrAl, SrGa, CaAl, CaGa, BaGa and BaSc are predicted to be stable. The parent

compound, SrSc is also predicted to be stable (within the errors of DFT) with an energy above the hull of 0.0005 eV atom^{-1}. CaSc and BaAl are predicted to be metastable with energies of 0.05 and 0.07 eV atom^{-1} respectively. CaSc and BaAl are expected to form but may not be phase pure when synthesised and as such other competing phases may be present. All the compounds where $A^{2+} = Mg$ and $M^{3+} = In$, Y, La were found to be unstable.

2.2. Geometric and Structural Properties

All thermodynamically stable compounds displayed the same *I4/mmm* crystal structure as the parent compound after relaxation.

Cell parameters: Table 1 displays the structural parameters for all the stable compounds and are grouped according to increasing radii of the M^{3+} cation (Al → Ga → Sc) and within these groups are ordered by increasing A^{2+} radii (Ca → Sr → Ba). The calculated lattice parameters and bond lengths for the parent compound, SrSc, are in excellent agreement with the experimental values[50] showing the efficacy of HSE06 to predict the structural properties of all 24 compounds. As expected when increasing the size of both A^{2+} and M^{3+} cations, the cell parameters, volumes and bond lengths all increase whilst retaining the *I4/mmm* crystal symmetry. In terms of volume change, within the Al, Ga and Sc compounds (Ca → Ba) an increase in volume by ∼20%, ∼18%, and ∼16%, is seen for each sub group respectively. The $a(c)$ parameters expand by ∼5(10)%, ∼4(10)%, and ∼3(9)% between Al, Ga and Sc respectively.

$[Cu_2S_2]^{2-}$ layer: Previous HSE06 studies carried out on SrSc[61] showed that the $[Cu_2S_2]^{2-}$ layer is responsible for the electronic states that form the VBM and are thus the most important for *p*-type conductivity. Comparable behaviour can be seen in the layered oxychalcogenides: LaCuOS and LaCuOSe which also possess a $[Cu_2Ch_2]^{2-}$ layer.[49] Figure 3 displays the change in valence band related bond lengths and angles comparative to the increasing basal lattice parameter (a). For each group, as is to be expected that through increasing the size of the cell there is a proportional increase in Cu–Cu, Cu–S, A^{2+}–S distances as well as S–Cu–S bond angles (in plane) for each group (Al, Ga, Sc). This allows for a general comparison of the basal lattice parameter (a) to the individual electronic and structural properties of the system. The Cu–Cu distances increase from 2.63 Å for CaAl to 2.94 Å for BaSc due to the increasing A^{2+} and the M^{3+} cationic radii. An increased Cu–Cu distance is typically preferable to avoid $d-d$ transitions which hamper the transparency of Cu-O based systems.[12] The Cu–S distances tend to plateau for Sr and Ba in each group (Al,Ga,Sc) and have a minimum bond length of 2.39 Å for CaAl and a maximum of 2.45 Å for BaSc. These results lie within the typical range of other copper

sulfide based materials such as Cu_2S ($\sim$2.27-2.35 Å)[62,63] as well as the layered oxysulfide LaCuOS ($\sim$2.42 Å).[48] It is likely that the Cu–S bond length restrains the systems from expanding further and hence partially dictates the stability of the $[Cu_2S_2][A_3M_2O_5]$ structure to accommodate the different variations. Judging from the increase in bond length from LaCuOS to LaCuOSe and even LaCuOTe[48,64,65] (2.42 $\rightarrow$ 2.52 $\rightarrow$ 2.66 Å) *selenide* or *telluride* based $[Cu_2S_2][A_3M_2O_5]$ systems may be able to accommodate the increasing cell size and hence larger A^{2+} and M^{3+} cations such as Y or La.

The S–Cu–S (in-plane) bond angles increase linearly with increasing *a* as expected from increasing the width of the unit cell producing a "concertina" effect on the $[Cu_2S_2]^{2-}$ layer. The calculated HSE06 value for SrSc (114.55∘) is in reasonable agreement with experiment, overestimating slightly by $\sim$ 5°.[50] The linear trend is broken slightly from SrSc to BaSc and is possible that a limit to the bond angle is occurring; any larger cells would likely become strained favouring either a different crystal structure, or the use of Se or Te within the $[Cu_2S_2]^{2-}$ layer. Cu_2S is known to have a S–Cu–S bond angle of 109.5°[62,63] and LaCuOS possesses one of 108.63°.[48]

The A^{2+}–S bond lengths were also calculated in order to establish an "interlayer spacing" between the two layers ($[Cu_2S_2]^{2-}$ and $[Sr_3Sc_2O_5]^{2+}$). Within each M^{3+} (Ca,Sr,Ba) group the increase is linear with respect to *a*, and to an extent *between* the different M^{3+} groups (Al,Ga,Sc). The maximum percentage increase within the Al, Ga and Sc groups is 8%, 7% and 5% respectively.

$[A_3M_2O_5]^{2+}$ layer: The average M^{3+}–O and A^{2+}–O bond lengths increase relative to both *a* and *c* lattice parameters within each M^{3+} group linearly. For the M^{3+}–O bond lengths, the analysis can be split into the effect of the *a* and *c* directions due to the tetrahedral bonding of M^{3+}. The different bond types are shown in Figure 1. Table 1 provides the values for both directions, and shows that in the *a* direction the bond length increases linearly with basal lattice parameter. As expected, M^{3+}–O increases proportionally with *a* between Al, Ga and Sc. The bond lengths in the *c* direction show little change between Ca, Sr and Ba however. Predictably the A^{2+}–O bond lengths increase as a function of their respective cell directions.

2.3. Electronic and Optical Properties

Density of States: Figure 4(a), (b) and (c) shows the total and partial density of states (DOS) for SrAl, SrGa and SrSc respectively which will be used as representatives of each group in this analysis. Table 2 displays the percentage of states at the VBM along with valence band widths (upper "uninterrupted" valence bands between -12eV and 0eV) and Table 3 display the percentage of

states at the CBM. Full plots of the partial and total DOS for all stable compounds are shown in SI Figure S1.

Within each M^{3+} group the composition of the upper valence band remains the same with only the valence band widths changing amongst the groups. Figure 4 a, b and c shows the DOS for SrAl, SrGa and SrSc which can be used to describe each M^{3+} group. In general the valence band widths decrease with increasing A^{2+} cation radius and are inversely proportional to the S–Cu–S angle. A more obtuse S–Cu–S angle therefore results in a smaller valence band width. In the same vein it would follow that the valence band width would decrease from SrAl → SrGa → SrSc due to the same increase in S–Cu–S angle due to the increasing size of M^{3+}, however this is not the case. As shown in Figure 4, both Al and Ga $s+p$ states are present from ∼ -10 eV to ∼ -7 eV. From -7 eV to ∼ -5 eV in SrAl and SrGa, significant mixing between O p, S p, Cu d and Al/Ga p states is seen. In SrSc, from -6 eV to -4 eV the majority of states in the valence band is made up of O p, S p, Cu d and Sc d states. From this point the compounds become very similar with a large proportion of the states belonging to Cu d mixed with O p states in a nearly 50:50 ratio from ∼ -3 eV to ∼ -2 eV. From -2 eV to the VBM (0 eV) Cu d states hybridise with S p states over O p almost exclusively in ∼ 55:∼ 41 Cu:S ratio with negligible contributions from Cu p, Sr $p+d$ and O p states (Table 2). These results are consistent with previous HSE06 calculations on SrSc.[61] as well as with the similar layered oxychalcogenides: LaCuOCh (where Ch=S,Se,Te).[66]

The states at the CBM are shown in Table 3 where the states vary with each group of compounds. Within the aluminium compounds, it is clear that a hybridisation between both the Cu s, S s and Al s and O s states generally make up the CBM. From Ca → Sr → Ba, the larger cell sizes increases the proportion of Al s states seen at the CBM from 5% → 14% → 30% respectively. A decrease in overall Cu and S states seen at the CBM is also observed making up 58% in SrAl to just 25% in BaAl. In CaAl, a significant mixing of Ca s states is present at the CBM, which could likely be due to the CaAl possessing the smallest A^{2+}–S bond length (2.97 Å). An increase in O $s+p$ states is observed down group 2. From the CBM to the peak at 4 eV in SrAl, the CBM consists of a hybridisation between the Cu s, Cu d and O p states mixed with predominantly Sr d states. From 4 eV to 6 eV the conduction band is primarily Sr d states mix with some O p and a small amount of Cu s states around 5.6 eV.

In the gallium systems, a reduction in the Cu s and S s states are seen at the CBM, with predominantly Ga s + Os mixing observed. Down group 2, an increase in the Ga s states is observed with a further reduction in the Cu and S states from 19% → 14% → 5% (from CaGa → SrGa → BaGa respectively). A similar effect is seen in the band alignment of AlN, GaN and InN where, due to

the increasingly penetrating s orbitals down the group means that the CBM lies lower in energy from AlN to GaN to InN.[67] From $\sim$2.7 eV to the peak at 4 eV, the conduction band of SrGa consists of an increasing hybridisation between the Ga s + O p states that make up the CBM and the Sr d, Cu $s + d$ and S p states. This is consistent with the peak at 4 eV in SrAl (Figure 4(a)) which possesses an increased Sr d presence. From 4 eV to 6 eV the CBM is predominantly Sr d states mixed with some O p, Cu s and Al s states.

The CBM of the scandium compounds consist of negligible quantities of Sc in contrast to the aluminium and gallium compounds. The CBM is predominantly Cu s and S $s+p$ with significant mixing from A^{2+} states. From Ca $\rightarrow$ Sr $\rightarrow$ Ba, the Cu s states increase from 21% to 34% in contrast to the Al and Ga compounds where increasing A^{2+} resulted in *less* Cu and S states at the CBM. Between CaSc and SrSc, a reduction in A^{2+} s states is observed. BaSc shows that the Ba d states dominate at the CBM with no S s or p states (as with CaSc and SrSc). This is likely due to the decreased Ba–Cu distance over Ca–Sc and Sr–Sc respectively due to the "concertina" effect of the $[Cu_2S_2]^{2-}$ layer and thus a more compact unit cell. In SrSc, the conduction band from the CBM to 6 eV consists of an increasing proportion of Sr d and Sc d states. Towards 6 eV an increased hybridisation with O p, S p and Cu s states is seen.

Band Structure and Optical Gap: The band structures of all stable $[Cu_2S_2][A_3M_2O_5]$ compounds are presented in Figure 5 and the direct, indirect and optical band gaps together with hole and electron effective masses at the VBM and CBM respectively are shown in Table 4. The value for the optical band gap is taken from the α^2 value (analagous to the Tauc relation: $(\alpha h\nu)^2$) in the absorption spectra compiled for each of the 9 compounds in SI Figure S3.

From our calculations, 3 of the 24 $[Cu_2S_2][A_3M_2O_5]$ compounds are found to be transparent: CaAl, SrSc and BaSc with optical band gaps of 3.17 eV, 3.06 eV and 3.24 eV respectively. The optical absorption for SrSc (3.06 eV) is in accordance with the optical band gap seen in experiment by Liu et al. who observed a band gap around 3.1 eV.[51] It is possible that SrAl will be transparent, however, colouring or haze may arise due to the 3.00 eV optical band gap. In general the optical band gaps correspond to the direct fundamental band gap at Γ, however for BaSc this is not the case. BaSc is the only compound to possess an *indirect* fundamental band gap where the VBM and CBM are located at Γ and X respectively. Due to the flat bands from Γ–X, the difference between the two high symmetry points is generally around 0.002 eV for each compound. The indirect and direct band gap at X (BaSc) is, however, a *disallowed* transition due to the d nature of both the VBM (Cu d) and CBM (Ba d). The direct band gap at Γ (3.20 eV) is, however, an allowed transition.

Figure 6(a) shows the change in direct fundamental band gap as a function

of a parameter. In both Al and Ga compounds the band gap shrinks as a function of increasing cell size. This can be attributed to the increased presence of Al and Ga s states at the CBM down from Ca $\rightarrow$ Sr $\rightarrow$ Ba from an increased interlayer spacing. Due to the larger penetration of the Ga 4s states over Al 3s, the CBM is lowered further in the gallium compounds over the aluminium compounds. The lower band gap, however does allow for a greater dispersion at the CBM and thus a lower electron effective mass as seen in both the band structures in Figure 5 and the effective masses in Table 4.

Conversely, the scandium compounds which see negligible Sc s and d states at the CBM (and appear around ~ 1 eV above the CBM in SrSc) show a widening of the fundamental band gap with increasing a parameter. The band gap, therefore is highly sensitive to the different states at the band maxima and minima and no one rule can be used to describe all compounds.

In order to possess high hole mobilities and thus produce degenerate p-type conductivity, the effective masses at the VBM must be low. For all 9 compounds there exists two degenerate bands at the VBM allowing for the calculation of a "heavy" and "light" effective mass (the Γ–X direction is amalgamated into one value due to the heavy nature of the holes in this direction). These values are presented in Table 4 and show that in the Γ–N and Γ–Z directions, the parent compound (SrSc) experiences heavy effective masses of $2.50\,m_e$ and $0.75\,m_e$ respectively. In the same directions, *light* hole effective masses of $0.45\,m_e$ and $0.73\,m_e$ are calculated respectively owing to the high mobilities at low carrier concentrations (for a p-type TC) seen in powder samples of $150\,\mathrm{cm^2\,V^{-1}\,s^{-1}}$.[51]

Figure 6(b) shows the trends of the hole effective masses as a function of a parameter for the Γ–N and Γ–Z directions for each group of compounds. For each group - aluminium, gallium and scandium compounds, the heavy effective masses in the Γ–N direction *decrease* as a function of increasing a size with maximum values of $4.54\,m_e$, $3.92\,m_e$ and $3.12\,m_e$ respectively and minimum values of $2.37\,m_e$, $2.21\,m_e$ and $1.90\,m_e$ respectively. In this direction the scandium compounds possess the lowest heavy hole effective masses in the Γ–N direction (BaSc $= 1.90\,m_e$).

The light hole effective masses in the Γ–N direction remain relatively constant in both the Al and Sc compounds with average effective masses of $0.37\,m_e$ and $0.344\,m_e$ respectively. The gallium compounds experience a slight decrease in magnitude from $0.37\,m_e$ for CaGa to $0.33\,m_e$ for BaGa. In reverse to the heavy hole effective masses seen in this direction, the Sc compounds display slightly higher effective masses compared to the Al and Ga compounds.

In the Γ–Z direction both heavy and light hole effective masses are low. From CaAl to BaAl, the heavy effective masses decrease from $0.81\,m_e \rightarrow 0.72\,m_e$ whilst the light hole masses remain around $\sim 0.55\,m_e$. In the gallium com-

pounds a decrease is seen in both the heavy and light effective masses with the highest effective mass being for CaGa ($0.70\,m_e$) and the lowest being for BaGa ($0.52\,m_e$). The heavy and light hole effective masses remain fairly similar in the scandium compounds with the exception of BaSc which displays a heavy and light effective mass of $0.72\,m_e$ and $0.63\,m_e$ respectively. From CaSc → SrSc → BaSc the effective masses decrease with increasing a parameter for both the heavy and light holes.

From Γ–X, however, the hole effective masses are very high (17.34 – $85.30\,m_e$) due to the very flat dispersion in the band structure (Figure 5). This is likely due to a lack of overlap between the Cu d and S p tetrahedra in the $[Cu_2S_2]^{2-}$ layers. The Γ–X direction corresponds to the ab plane (SI Figure S2 shows the first Brillouin zone) and hence with an increasing "flattening" of this layer due to the more obtuse S–Cu–S angles with larger cation sizes, it is expected that a better overlap between Cu and S will occur and thus lower hole effective masses in the Γ–X direction. This effect is certainly the case for both the aluminium and gallium compounds where the effective masses reduces from $85.31\,m_e \rightarrow 17.34\,m_e$ and $85.31\,m_e \rightarrow 31.30\,m_e$ respectively. The scandium compounds, however, do not see the same trend with the largest values seen for SrSc. Due to the very high mobilities ($150\,cm^2\,V^{-1}\,s^{-1}$).[51] seen in experiment, it is likely that this effective mass in the Γ–X direction does not limit the mobilities as much as the Γ–N and Γ–Z directions do.

In general the *electron* effective masses in all directions decrease as a function of increasing a parameter. Due to the lower lying CBM in the gallium compounds, the lowest electron effective mass is seen for BaGa with an average effective mass of $0.20\,m_e$ competitive with the industry standard n-type TCs such as In_2O_3 ($0.22\,m_e$).[68] In the scandium compounds, the trend is broken due to the Ba d states forming an indirect band gap with the CBM at X. BaSc therefore possesses the highest electron effective masses of $0.95\,m_e$ (X–Γ) and $0.35\,m_e$ (X–P) out of the stable compounds.

3. Dynamic Stability

To further analyse the dynamic stability of the predicted structures the phonon dispersion curves were calculated using 3 × 3 × 2 supercells (252 atoms) and the finite displacement method[69,70] as implemented in Phonopy.[71]

It was found that for the three TC compounds (BaSc, SrSc and CaAl) that no imaginary modes appeared at Γ indicating that each structure is dynamically stable, however in both the SrSc and CaAl structures imaginary acoustic modes appear around N and Z for SrSc and just at N for CaAl indicating that these

might not be the ground state structures at lower temperatures.

These can be indicative of potential structural distortions to reach another structural phase which is lower in energy, however the *I4/mmm* structure may likely be stable at room temperature as is the case with SrSc.

4. Calculated Conductivity

Using Boltzmann transport theory, the *p*-type conductivities for BaSc, SrSc and CaAl were calculated at varying carrier concentrations using HSE06. From our calculations we find that BaSc has the highest *p*-type conductivity of 2058 S cm^{-1} followed by CaAl (1767 S cm^{-1}) and SrSc (1673 S cm^{-1}) at a carrier density of 1×10^{21} cm^{-3} and are shown in Figure 8. These results compare well with the calculated average hole effective masses which show that BaSc should have a higher mobility and thus a larger conductivity to CaAl and SrSc. In experiment, powder samples of $[Cu_2S_2][Sr_3Sc_2O_5]$ displayed undoped conductivities of 2.8 S cm^{-1} from a carrier concentration of $\sim 10^{17}$ cm^{-3}.[51] From the Boltztrap calculations we find that for a carrier concentration of 1×10^{18} cm^{-3} gives a conductivity of 2.03 S cm^{-1}. It is likely that for a powder sample, the accuracy of the carrier concentrations determined from Hall effect may be questioned due to the grain boundaries, however these results help to validate the use of Boltztrap to determine the conductivity of these compounds.

These values are significantly larger than the highest reported *p*-type conductivity of 220 S cm^{-1} which was found for Mg doped $CuCrO_2$ [36] making BaSc potentially the highest performing p-type TC to date. Analysis of the defect chemistry of BaSc would, however, be required to determine whether a high carrier concentration can be reached for BaSc and the optimum dopant necessary to facilitate this. For comparison, the industry standard *n*-type TCs are presented in Figure 8 alongside experimental values for Sn-doped In_2O_3, Al/Ga-doped ZnO and F/Sb/Ta-doped SnO_2 for carrier concentrations $\sim 1\times10^{21}$ cm^{-3}. Although the *p*-type conductivities aren't of the same order as the *n*-type TCs, the significant enhancement in conductivity from BaSc drastically closes the gap.

5. Experimental Results

To validate our predictions, we have prepared a sample of $[Cu_2S_2][Ba_3Sc_2O_5]$ by direct combination of BaO, Sc_2O_3 Cu_2S and BaS. This yielded a light brown powder, with a crystalline diffraction pattern.

5.1. XRD

The powder XRD diffraction pattern of $[Cu_2S_2][Ba_3Sc_2O_5]$ is shown in Figure 9. A Rietveld refinement was carried out against these data using a starting model based on the previously reported and assumed isostructural $[Cu_2S_2][Sr_3Sc_2O_5]$, but with replacement of strontium ions with barium ions and an appropriate expansion in lattice parameter. Refinement of this model against the data was carried out with refinement of the background function, the Lorentzian and Gaussian components of pseudo-Voight peak-profile functions, the lattice parameters, the atomic positions and their isotropic displacements. The refinement confirmed that $[Cu_2S_2][Ba_3Sc_2O_5]$ was single phase crystallising in the tetragonal *I4/mmm* space group with lattice parameters of $a = 4.14462(2)$Å and c,$= 27.12390(8)$Å, with a good fit to the data with $\chi^2 = 2.938$ and $R_p =$ 7.80%. The final structural model is given in SI Table S7. All the structural parameters are given in Table 5.

All structural properties are within excellent agreement with the calculated HSE06 values by $<2\,\%$ with a slight overestimation of the c direction.

5.2. Optical Absorption

Spectroscopic diffuse reflection data were recorded on the sample of $[Cu_2S_2][Ba_3Sc_2O_5]$, and used to produce a Tauc plot which can be seen in Figure 10. This shows a strong absorption which can be attributed to a direct band gap of 3.24 eV. This puts the band gap in the UV, and therefore we would predict that the material should be transparent, which is contradicted by the observed light brown colour of the powder. However, there is an additional, less intense feature in the plot which can be related to a band gap of 2.26 eV, which is more consistent with the observed colour. The origin of this is still not clear, but could be due to an amorphous impurity or d–d transitions within Cu related defects.

5.3. Discussion

From our analysis, two potential *p*-type transparent conductors have been predicted using hybrid density functional theory. These compounds are CaAl and BaSc with optical band gaps of 3.17 eV and 3.24 eV respectively. The synthesis of BaSc powders confirm the predictions gained from DFT in particular the wide optical band gap making BaSc a potential *p*-type transparent conductor. From the structural analysis, a clear trend can be seen based on the a lattice parameter. With increasing cell size, a narrowing of the $[Cu_2S_2]^{2-}$ layer is seen which influences the curvature and width of the valence band and thus directly

affects the electronic properties. In the delafossite Cu^{1+} oxides, it was found that conductivity can be loosely proportional to the Cu–Cu distances due to the relatively flat VBM.

A small distance was required to reduce the "hopping" distance thus higher undoped conductivities were seen for $CuBO_2$ over $CuAlO_2$.[46,61] We find that in the $[Cu_2S_2][A_3M_2O_5]$ materials, an increased a parameter (corresponding to an extended Cu–Cu distance) *decreases* the overall effective masses seen in the Γ–Z and Γ–N directions (however with an increase in the heavy hole masses in the scandium compounds). This behaviour is seen to exist in the other layered oxychalcogenides LaCuOS and LaCuOSe where a larger Cu–Cu distance is not detrimental to the conductivity.[49,61] The larger Cu–Cu distances also inhibit $d-d$ transitions which could limit the transparency. Out of the new predicted potential TCs, the lowest hole effective masses were seen for BaSc making this the most promising discovery from this work.

In order for $[Cu_2S_2][Ba_3Sc_2O_5]$ to be a successful p-type TC it would need to achieve large carrier concentrations from intrinsic defects such as vacancies and antisites (e.g. V_{Cu} or Sr_{Sc}) or through extrinsic doping for high p-type conductivity. Judging from the conductivities found by Liu et al. of $2.8\,S\,cm^{-1}$ for undoped powders of $[Cu_2S_2][Sr_3Sc_2O_5]$, it is likely that shallow intrinsic acceptor defects could be present in the BaSc analogue. A full analysis of the intrinsic defect chemistry is beyond the scope of this present study due to the sheer number of defect types and charge states to consider. Speculation on the possible defects can be made by drawing parallels to an already studied layered oxychalcogenide system such as LaCuOSe. In this material, it was found that the intrinsic defects do not fully account for the high conductivities as the lowest formation energy acceptor, V_{Cu} has a modest ionisation energy of $\sim$ 0.1 eV,[49] however under p-type favourable growth conditions (a *Se/O-rich* regime) there is a relatively large dopability window where minimal compensation occurs. This is seen in the high reported p-type conductivity from Mg doping ($\sim 910\,S\,cm^{-1}$ [47]). If a similar situation arises in $[Cu_2S_2][Ba_3Sc_2O_5]$ enhanced p-type conductivity can be expected by doping with group I cations, for example, without intrinsic or self-compensation.[5]

Additionally, the polaronic binding energy of holes can be calculated for $[Cu_2S_2][Ba_3Sc_2O_5]$ and $[Cu_2S_2][Sr_3Sc_2O_5]$ giving rise to values of 0.04 eV and 0.08 eV respectively within the ab plane. It is clear that $[Cu_2S_2][Ba_3Sc_2O_5]$ will be a better p-type conductor than $[Cu_2S_2][Sr_3Sc_2O_5]$ however, whilst these values are slightly above any room temperature excitation ($\sim$0.03eV at k_BT at 300K) it can be expected that excitation could occur from photons with wavelengths greater than mid-IR.[72]

It is also important to understand whether such carrier concentrations

would be detrimental to the optical absorption. As such, transitions from below the VBM were calculated to simulate the effect of hole doping on the optical properties of BaSc using the method outlined in ref. [37]. The optical spectrum can be found in SI Figure S4 and shows that visible light absorption is negligible, with the significant transitions occurring in the near-IR suggesting that BaSc will remain a transparent p-type conductor upon doping, similar to $[Cu_2S_2][Sr_3Sc_2O_5]$[37].

Optimising the band gap in the $[Cu_2S_2][A_3M_2O_5]$ layered oxychalcogenides is based upon two observations. Firstly, a smaller valence band width could play a role in improving the magnitude of the band gap. In general it was seen that a larger Cu–Cu distance resulted in a smaller VB width which could explain the increase in band gap seen in the scandium compounds (where the CBM is not influenced by M^{3+} states). Secondly, the states that make up the CBM highly influence the position of the conduction band. In the aluminium and gallium compounds, the low lying M^{3+} *s* states cause a sharp reduction in the band gap. The position of the conduction band is highly sensitive to the M^{3+}–O bond length thus larger cells push the CBM lower in energy. Despite this, increasing the cell size reduces the VBM effective mass so a compromise is necessary for a wide band gap, high mobility TC. In both the aluminium and scandium compounds there is significant mixing of the Cu and S states at the CBM which could enhance the transparency which can be seen by the decrease in fundamental band gap with increasing percentage of Cu and S states at the CBM. The decrease in band gap in the aluminium compounds with increasing *a* is similar to other layered oxychalcogenides such as LaCuOSe (2.82 eV[17]), SmOCuSe (2.60 eV[73]) and YOCuSe (2.58 eV[74]) however the scandium $[Cu_2S_2][A_3M_2O_5]$ compounds see the reverse.

Aside from the parent compound (SrSc), six other compounds were found to be stable albeit without band gaps wide enough to accommodate high optical transparencies. It is possible, however, that these materials could be used in other applications such as photovoltaics or photocatalysis. SrGa for example, displays a band gap in the correct range for a solar absorber (E_g^{opt}=1.71 eV).[75] Despite this, the optical absorption onset is fairly weak. It could be possible, however to create an alloyed oxychalcogenide such as Sr/BaGa or BaAl/BaGa to reduce the band gap or create a stronger absorption.[76] CaGa and BaAl both have band gaps in the range of a visible light water-splitter[77] (2.01 eV and 2.42 eV respectively), however, due to the metastability of BaAl, only CaGa can be recommended for photocatalytic water splitting. Further work would require band alignment and surface calculation to determine whether CaGa would be successful in this application.

It is likely that the thermodynamic stability of the compounds are restricted

by certain structural parameters such as the volume, S–Cu–S bond angles and Cu–S bond lengths, thus going from S to Se to Te could help accommodate a smaller or larger cell size such as the Mg or La cells which were found to be unstable from this work. In terms of cell volume, the smallest analogue found synthesised under atmospheric pressure is $[Cu_2S_2][Sr_3Fe_2O_5]$[78] which possessed a volume of 402.69 Å^3; smaller volumes were attainable for $[Fe_2(P,As)_2][Ca_3Al_2O_5]$[79] (348.29 Å^3 and 365.16 Å^3 respectively), however these were synthesised at 4.5 GPa. These known limits could give rise to difficulties in atmospheric pressure synthesis of the Al compounds.

Comparing LaCuOS, LaCuOSe and LaCuOTe, the S–Cu–S bond angles decrease from 111.2° → 107.5° → 103.5° respectively, however the Cu–S bond lengths increase from 2.42 Å → 2.52 Å → 2.66 Å respectively.[66] It is expected that the VBM dispersion will increase down the chalcogenides as seen with the increased conductivity from LaCuOS to LaCuOSe.[49] Including Se and Te however, may have a detrimental effect on the optical band gap as can be seen in other layered oxychalcogenides such as LaCuOCh[17,47,65,80] and other layered Cu–Chalcogen structures such as BaFCuS (3.2 eV[81], BaFCuSe (2.9 eV[82]) and BaFCuTe (2.3 eV[83]).[74] It is likely, however, that combining the design rules laid out here that transparency with a selenide or telluride may be possible, i.e. $[Cu_2Se_2][(Y/La)_2Al_2O_5]$. Other known layered Cu^{1+} oxychalcogenide structures such as $[CuS][Sr_2GaO_3]$[84], $[Cu_2S_2][Bi_2YO_4]$[85] or $[Cu_2S_2][Sr_2(Mn/Zn)O_2]$[86,87] to name a few, could also be explored in the same way.

The prediction of a potential high-conductivity *p*-type transparent conductor has been achieved using a thermodynamic stability screening guided by chemical knowledge using density functional theory. Based on the $[Cu_2S_2][Sr_3Sc_2O_5]$ structure, 24 compounds were proposed, 8 of which were found to be stable and to possess semiconductor properties. The compound $[Cu_2S_2][Ba_3Sc_2O_5]$ was found to possess a wide optical band gap (E_g^{opt} = 3.24 eV) and high calculated *p*-type conductivities ($\sim$ 2058 S cm^{-1}) which is in the conductivity range of thin films of industry standard *n*-type TCs and the largest predicted for any *p*-type TC. Synthesized powders of $[Cu_2S_2][Ba_3Sc_2O_5]$ confirmed the structural and optical properties predicted using hybrid DFT. This work paves the way for the design of higher mobility *p*-type TCs increasing the possibility of transparent electronics.

6. Computational and Experimental Procedures

6.1. Computational Methodology

Ab-initio calculations using VASP code[88–91] were performed using both standard and hybrid functionals. Variations of the $[Cu_2S_2][A_3M_2O_5]$ structure (tetragonal, *I4/mmm*) were formed where A=**Sr**,Ca,Ba,Mg and M=**Sc**,Al,Ga,In,Y,La. This resulted in 24 compounds with the same stoichiometry as $[Cu_2S_2][Sr_3Sc_2O_5]$ and are named using the convention "AB" eg. $[Cu_2S_2][Sr_3Sc_2O_5]$ is "SrSc" and $[Cu_2S_2][Ba_3Al_2O_5]$ is "BaAl". These compounds were relaxed using the PBEsol[92] (Perdew-Burke-Ernzerhoff revised for solids) functional with a Hubbard-like U correction value of 5.17 eV for Cu.[37] The projector-augmented wave method (PAW)[93] was used to describe the interactions between the core electrons and valence electrons which are treated explicitly. The 24 compounds were relaxed using a plane wave energy cut-off of 500 eV to avoid Pulay stress[94] and a $6 \times 6 \times 2$ Γ-centred k-point mesh for accuracy. Convergence was deemed complete when the forces acting on all the ions was less than 0.01 eV Å^{-1}.

In order to screen the novel compounds in terms of their thermodynamic stability, all known competing phases and elements related to the quinary systems were also calculated using PBEsol+U (Supplementary Information (SI) Tables S1 and S2). This resulted in the calculation of $\sim$ 313 crystal structures from the ICSD[59] alongside calculating the lowest energy magnetic orderings for each of the Cu^{2+}-containing compounds. A standard 500 eV plane-wave energy cutoff was employed to allow for total convergence of these systems together with k-point meshes generated to allow a sampling density of 0.04 Å^{-1} which was found to be sufficiently accurate. The *Chemical Potential Limits Analysis Program* (CPLAP)[95] code was used to assess the thermodynamic stability of the 24 $[Cu_2S_2][A_3M_2O_5]$ compounds as well as evaluating the energy above the convex hull for the unstable compounds.

The stable and metastable compounds were then subjected to an HSE06 (Heyd-Scuzeria-Ernzerhoff)[96] relaxation in order to glean accurate electronic and optical properties. The HSE06 hybrid functional has been shown to give a correct description of the band gap and optical properties of SCSOS[61] relative to experiment.[51] The optical absorption spectra were calculated using the real and imaginary parts of the dielectric constant calculated using a Kramers-Kronig transformation and a summation over the unoccupied bands respectively using a method by Furthmüller and coworkers.[97] This sums the absorption spectrum over *all* direct valence band to conduction band transitions ignoring intraband and indirect absorptions.

The effective masses of the valence and conduction band extrema are calculated using the relationship:

$$\frac{1}{m^*_{ij}} = \frac{\delta^2 E(k)}{\delta k_i \delta k_j} \frac{1}{\hbar^2} \tag{1}$$

where $E(k)$ is defined as the eigenvalue of the band at a specific k and m^*_{ij} as the effective mass.

Phonon dispersions were calculated with Phonopy[71] using the finite displacement method and $3 \times 3 \times 2$ supercells (252 atoms) generated from the optimised structure. The optimised structure was minimised using PBEsol with a force convergence criterion of 1×10^{-3} and the electronic wavefunction converged to 1×10^{-8}.

Electrical conductivity values were calculated using Boltzmann transport theory within the BoltzTraP[98] code. A dense Γ-centred $13 \times 13 \times 4$ k-point mesh was deemed sufficient for use (HSE06) within VASP which can be read by BoltzTrap. The calculated conductivity represents a theoretical maximumw with the scattering processes treated by the relaxation time approximation.

The polaron binding energy ($E_{polaron}$) can be calculated using the formalism laid out by Fröhlich[72,99,100]:

$$E_{polaron} = \frac{1}{8\pi^2} \frac{m^* e^4}{\hbar^2 \epsilon^2_{eff}} \tag{2}$$

where:

$$\frac{1}{\epsilon_{eff}} = \left(\frac{1}{\epsilon_\infty} - \frac{1}{\epsilon_0}\right) \tag{3}$$

where ϵ_∞ and ϵ_0 are the optical high-frequency dielectric constant and the low dielectric constants respectively.

The open source python package *sumo*[101] (github.com/SMTG-UCL/sumo) by Ganose et al. was used in the production of the density of states, electronic band structures, optical absorption and phonon dispersion plots.

6.2. Experimental Methodology

6.2.1. Solid-State Synthesis:

Sc_2O_3 (99.99% , Alfa Aesar) and Cu_2S (99.5% , Alfa Aesar) were purchased and used as supplied. BaO was prepared via the thermal decomposition of $BaCO_3$ (99% . Alfa Aesar) under dynamic vacuum (1000°C, 14 h) in a silica tube closed at one end, before being stored in a nitrogen filled glovebox (Saffron). BaS was

synthesised by reaction of CS_2 vapour with $BaCO_3$ (900°C, 8 h). The CS_2 vapour was generated by flowing argon (Pureshield, 99.998% , BOC) through a bubbler containing liquid CS_2 (99.9% , Sigma Aldrich). After the vapour exited the reactor it was passed through two hydroxide-bleach containing bubblers in order to oxidise any excess CS_2 or H_2S. The purity of these precursors was confirmed by powder X-ray diffraction. A 0.5 g powder sample of $[Cu_2S_2][Ba_3Sc_2O_5]$ was synthesised by reaction of BaO, BaS, Sc_2O_3 and Cu_2S in a 2:1:1:1 stoichiometric ratio. Desired precursor amounts were weighed, mixed and ground in an agate pestle and mortar under an inert atmosphere in a glovebox. The precursor mixture was then loaded into a die (13mm, Specac), removed from the glove box, pressed into a pellet and immediately returned to the inert atmosphere. The pellet was loaded into an alumina crucible which was then sealed under vacuum in a silica ampoule. The sealed sample was heat treated at 800°C for 12 hours. The sample was ground, re-pelleted and resealed in an alumina crucible in a silica ampoule with 2 further heat treatments at 800°C for 12 hours. Sample purity was monitored using powder X-ray diffraction (PXRD), and once synthesized the sample was found to be air stable by detection limits of lab PXRD.

6.2.2. X-ray Diffraction:

The purity of precursors and initial phase identification of the targeted product was confirmed by X-ray diffraction using a Bruker D2 in Bragg-Brentano geometry with a Cu Kα X-ray source (20 kV; 10 mA). Full characterisation of the compound $[Cu_2S_2][Ba_3Sc_2O_5]$ was performed using synchrotron X-ray diffraction data collected from the I11 beamline, Diamond Light Source, using 15 keV X-rays (0.82603Å) over a range $10<2\theta<100°$, with a step size of 0.001° and with a scan rate of 2.5° min^{-1}. Rietveld refinement of structural models against these data was carried out using the GSAS suite of software, with the EXPGUI interface.[102]

6.2.3. Spectrophotometry:

Diffuse reflectance measurements were collected using a UV-Vis-near IR Spectrophotometer (Perkin-Elmer Lambda 750 S) using deuterium and tungsten lamps and equipped with a 100 mm integrating sphere. Diffuse reflectance data were converted into the Kubelka-Munk function, f(R),[103] assumed proportional to the absorption coefficient throughout the visible region, which was used in the construction of a Tauc plot.[104,105] The band gap was estimated by determining the x-axis intercept of a linear fit of the absorption edge. This was

fitted by the plotting of a linear function passing through the two data points between which the largest gradient was observed.

Acknowledgements

BADW would like to acknowledge useful discussions with Dr A. M. Ganose, Dr C. N. Savory and Dr. D. W. Davies. BADW would like to acknowledge Mr K. Spooner for his assistance in the *n*-type TC Boltztrap data. GJL would like to acknowledge experimental support of Mr D. Salazar-Marcano, Mr P. Bayliss and Mr N. Davis. Thankyou to Mr C Tang for performing the synchrotron diffraction experiment. GJL and GH would also like to thank Prof. G. Reid and Prof. A. Hector, and Dr D. Bradshaw and Dr S. Cosham for useful discussions. This work made use of the ARCHER UK National Supercomputing Service (http://www.archer.ac.uk) via our membership of the UK's HEC Materials Chemistry Consortium, which is also funded by the EPSRC (EP/L000202). The UCL Legion and Grace HPC Facilities (Legion@UCL and Grace@UCL) were also used in the completion of this work. GJL and GH would like to acknowledge use of the Diamond I11 Rapid Access beamtime: EE16644. DOS would like to acknowledge support from the EPSRC (EP/N01572X/1) and BADW and DOS would like to acknowledge support from the European Research Council, ERC, (Grant 758345). DOS acknowledge membership of the Materials Design Network.

Author Contributions

DOS conceived the idea and designed the project, BADW carried out all the computational simulations with the exception of the optical absorption calculations $[Cu_2S_2][Ba_3Sc_2O_5]$ with a hole in the valence band which were performed by GWW, GJL and GH undertook all of the solid state synthesis, spectroscopy and analysis. All authors contributed to the writing of the manuscript and gave approval to the final version of the manuscript.

Declaration of Interest

The authors declare no conflicts of interest.

[1] K. H. L. Zhang, K. Xi, M. G. Blamire, R. G. Egdell, P-type transparent conducting oxides, Journal of Physics: Condensed Matter 28 (38) (2016) 383002.

[2] J. C. C. Fan, F. J. Bachner, G. H. Foley, Effect of o_2 pressure during deposition on properties of rf-sputtered sn-doped in_2o_3 films, Applied Physics Letters 31 (11) (1977) 773–775.

[3] D. S. Bhachu, D. O. Scanlon, G. Sankar, T. D. Veal, R. G. Egdell, G. Cibin, A. J. Dent, C. E. Knapp, C. J. Carmalt, I. P. Parkin, Origin of high mobility in molybdenum-doped indium oxide, Chemistry of Materials 27 (8) (2015) 2788–2796.

[4] M. Oshima, K. Yoshino, Characteristic of low resistivity fluorine-doped sno_2 thin films grown by spray pyrolysis, Japanese Journal of Applied Physics 50 (5) (2011) 05FB15.

[5] J. E. N. Swallow, B. A. D. Williamson, T. J. Whittles, M. Birkett, T. J. Featherstone, N. Peng, A. Abbott, M. Farnworth, K. J. Cheetham, P. Warren, D. O. Scanlon, V. R. Dhanak, T. D. Veal, Self-compensation in transparent conducting f-doped sno_2, Advanced Functional Materials (2017) 1701900.

[6] S. D. Ponja, B. A. D. Williamson, S. Sathasivam, D. O. Scanlon, I. P. Parkin, C. J. Carmalt, Enhanced electrical properties of antimony doped tin oxide thin films deposited via aerosol assisted chemical vapour deposition, Journal of Materials Chemistry C 6 (27) (2018) 7257–7266.

[7] M. J. Powell, B. A. D. Williamson, S.-Y. Baek, J. Manzi, D. B. Potter, D. O. Scanlon, C. J. Carmalt, Phosphorus doped SnO2 thin films for transparent conducting oxide applications: synthesis, optoelectronic properties and computational models, Chemical Science 9 (41) (2018) 7968–7980.

[8] H. Agura, A. Suzuki, T. Matsushita, T. Aoki, M. Okuda, Low resistivity transparent conducting al-doped ZnO films prepared by pulsed laser deposition, Thin Solid Films 445 (2) (2003) 263–267.

[9] S. C. Dixon, S. Sathasivam, B. A. D. Williamson, D. O. Scanlon, C. J. Carmalt, I. P. Parkin, Transparent conducting n-type ZnO:sc – synthesis, optoelectronic properties and theoretical insight, Journal of Materials Chemistry C 5 (30) (2017) 7585–7597.

[10] S. Sallis, D. O. Scanlon, S. C. Chae, N. F. Quackenbush, D. A. Fischer, J. C. Woicik, J.-H. Guo, S. W. Cheong, L. F. J. Piper, La-doped $basno_3$ - degenerate perovskite transparent conducting oxide: Evidence from synchrotron x-ray spectroscopy, Applied Physics Letters 103 (4) (2013) 042105.

[11] D. O. Scanlon, Defect engineering of $basno_3$ for high-performance transparent conducting oxide applications, Physical Review B 87 (16) (2013) 161201.

[12] H. Kawazoe, M. Yasukawa, H. Hyodo, M. Kurita, H. Yanagi, H. Hosono, P-Type Electrical Conduction in Transparent Thin Films of $CuAlO_2$, Nature 389 (6654) (1997) 939–942.

[13] H. Hiramatsu, K. Ueda, H. Ohta, M. Hirano, T. Kamiya, H. Hosono, Wide gap p-type degenerate semiconductor: Mg-doped LaCuOSe, Thin Solid Films 445 (03) (2003) 304–308.

[14] A. Zakutayev, T. R. Paudel, P. F. Ndione, J. D. Perkins, S. Lany, A. Zunger, D. S. Ginley, Cation off-stoichiometry leads to high p-type conductivity and enhanced transparency in co_2zno_4 and co_2nio_4 thin films, Physical Review B 85 (8).

[15] J. Fan, K. Sreekanth, Z. Xie, S. Chang, K. Rao, p-type ZnO materials: Theory, growth, properties and devices, Progress in Materials Science 58 (6) (2013) 874–985.

[16] B. A. D. Williamson, J. Buckeridge, J. Brown, S. Ansbro, R. G. Palgrave, D. O. Scanlon, Engineering valence band dispersion for high mobility p-type semiconductors, Chemistry of Materials 29 (6) (2016) 2402–2413.

[17] H. Hiramatsu, K. Ueda, H. Ohta, M. Hirano, T. Kamiya, H. Hosono, Degenerate p-type conductivity in wide-gap $lacuos_{1-x}se_x$ (x=0–1) epitaxial films, Applied Physics Letters 82 (7) (2003) 1048–1050.

[18] H. Mizoguchi, M. Hirano, S. Fujitsu, T. Takeuchi, K. Ueda, H. Hosono, $Znrh_2o_4$: A p-type semiconducting oxide with a valence band composed of a low spin state of rh^{3+}in a $4d^6$ configuration, Applied Physics Letters 80 (7) (2002) 1207–1209.

[19] G. Brauer, J. Kuriplach, C. C. Ling, A. B. Djurišić, Activities towards p-type doping of ZnO, Journal of Physics: Conference Series 265 (2011) 012002.

[20] M. Suja, S. B. Bashar, M. M. Morshed, J. Liu, Realization of cu-doped p-type ZnO thin films by molecular beam epitaxy, ACS Applied Materials & Interfaces 7 (16) (2015) 8894–8899.

[21] H. Pan, X. Meng, J. Cai, S. Li, G. Qin, 4d transition-metal doped hematite for enhancing photoelectrochemical activity: Theoretical prediction and experimental confirmation, RSC Advances 5 (25) (2015) 19353–19361.

[22] C.-Y. Tsay, S.-C. Liang, Fabrication of p-type conductivity in sno_2 thin films through ga doping, Journal of Alloys and Compounds 622 (2015) 644–650.

[23] S. S. Pan, G. H. Li, L. B. Wang, Y. D. Shen, Y. Wang, T. Mei, X. Hu, Atomic nitrogen doping and p-type conduction in sno_2, Applied Physics Letters 95 (22) (2009) 222112.

[24] S. S. Pan, S. Wang, Y. X. Zhang, Y. Y. Luo, F. Y. Kong, S. C. Xu, J. M. Xu, G. H. Li, P-type conduction in nitrogen-doped sno_2 films grown by thermal processing of tin nitride films, Applied Physics A 109 (2) (2012) 267–271.

[25] J. Asbalter, A. Subrahmanyam, P-type transparent conducting in_2o_3-ag_2o thin films prepared by reactive electron beam evaporation technique, Journal of Vacuum Science & Technology A: Vacuum, Surfaces, and Films 18 (4) (2000) 1672–1676.

[26] Y. Li, J. Sun, D. J. Singh, Infrared absorption and visible transparency in heavily doped p-type $basno_3$, Applied Physics Letters 110 (5) (2017) 051904.

[27] C. L. Hsin, J. H. He, C. Y. Lee, W. W. Wu, P. H. Yeh, L. J. Chen, Z. L. Wang, Lateral self-aligned p-type in_2o_3 nanowire arrays epitaxially grown on si substrates, Nano Letters 7 (6) (2007) 1799–1803.

[28] J. D. Perkins, T. R. Paudel, A. Zakutayev, P. F. Ndione, P. A. Parilla, D. L. Young, S. Lany, D. S. Ginley, A. Zunger, N. H. Perry, Y. Tang, M. Grayson, T. O. Mason, J. S. Bettinger, Y. Shi, M. F. Toney, Inverse design approach to hole doping in ternary oxides: Enhancing p-type conductivity in cobalt oxide spinels, Physical Review B 84 (20) (2011) 205207.

[29] H. J. Kim, I. C. Song, J. H. Sim, H. Kim, D. Kim, Y. E. Ihm, W. K. Choo, Electrical and magnetic properties of spinel-type magnetic semiconductor ZnCo2o4 grown by reactive magnetron sputtering, Journal of Applied Physics 95 (11) (2004) 7387–7389.

[30] H. Kawazoe, H. Yanagi, K. Ueda, H. Hosono, Transparent p-type conducting oxides: Design and fabrication of p-n heterojunctions, MRS Bulletin 25 (08) (2000) 28–36.

[31] A. Ievtushenko, O. Khyzhun, I. Shtepliuk, O. Bykov, R. Jakieła, S. Tkach, E. Kuzmenko, V. Baturin, O.Karpenko, O. Olifan, G. Lashkarev, X-ray photoelectron spectroscopy study of highly-doped zno:al,n films grown at o-rich conditions, Journal of Alloys and Compounds 722 (2017) 683–689.

[32] M. a. Marquardt, N. a. Ashmore, D. P. Cann, Crystal Chemistry and Electrical Properties of the Delafossite Structure, Thin Solid Films 496 (1) (2006) 146–156.

[33] K. Ueda, T. Hase, H. Yanagi, H. Kawazoe, H. Hosono, H. Ohta, M. Orita, M. Hirano, Epitaxial Growth of Transparent *p*-Type Conducting $CuGaO_2$ Thin Films on Sapphire (001) Substrates by Pulsed Laser Deposition, Journal of Applied Physics 89 (3) (2001) 1790.

[34] M.-S. Miao, S. Yarbro, P. T. Barton, R. Seshadri, Electron affinities and ionization energies of cu and ag delafossite compounds: A hybrid functional study, Physical Review B 89 (4) (2014) 045306.

[35] H. C. Kandpal, R. Seshadri, First-principles electronic structure of the delafossites abo_2 (a = cu, ag, au; b = al, ga, sc, in, y): Evolution of d^{10}–d^{10} interactions, Solid State Sciences 4 (8) (2002) 1045–1052.

[36] R. Nagarajan, a. D. Draeseke, a. W. Sleight, J. Tate, p-Type Conductivity in $CuCr_{1-x}Mg_xO_2$ Films and Powders, Journal of Applied Physics 89 (2001) (2001) 8022–8025.

[37] D. O. Scanlon, G. W. Watson, $(cu_2s_2)(sr_3sc_2o_5)$-a layered, direct band gap, *p*-type transparent conducting oxychalcogenide: A theoretical analysis., Chemistry of Materials 21 (22) (2009) 5435–5442.

[38] M. Snure, A. Tiwari, $CuBO_2$: A *p*-Type Transparent Oxide, Applied Physics Letters 91 (9) (2007) 092123.

[39] L.-J. Shi, Z.-J. Fang, J. Li, First-principles study of p-type transparent conductive oxides CuXO[sub 2] (x=y, sc, and al), Journal of Applied Physics 104 (7) (2008) 073527.

[40] K. G. Godinho, J. J. Carey, B. J. Morgan, D. O. Scanlon, G. W. Watson, Understanding Conductivity in $SrCu_2O_2$: Stability, Geometry and Electronic Structure of Intrinsic Defects from First Principles, Journal of Materials Chemistry 20 (6) (2010) 1086–1096.

[41] A. Kudo, H. Yanagi, H. Hosono, H. Kawazoe, $SrCu_2O_2$: A *p*-Type Conductive Oxide with Wide Band Gap, Applied Physics Letters 73 (2) (1998) 220.

[42] D. O. Scanlon, G. W. Watson, Conductivity Limits in $CuAlO_2$ from Screened-Hybrid density functional theory, Journal of Physical Chemistry Letters 1 (21) (2010) 3195–3199.

[43] D. O. Scanlon, G. W. Watson, Understanding the *p*-type defect chemistry of $cucro_2$, Journal of Materials Chemistry 21 (11) (2011) 3655.

[44] S. Kashida, W. Shimosaka, M. Mori, D. Yoshimura, Valence band photoemission study of the copper chalcogenide compounds, cu_2s, cu_2se and cu_2te, Journal of Physics and Chemistry of Solids 64 (12) (2003) 2357–2363.

[45] Y. Wu, C. Wadia, W. Ma, B. Sadtler, A. P. Alivisatos, Synthesis and photovoltaic application of copper(i) sulfide nanocrystals, Nano Letters 8 (8) (2008) 2551–2555.

[46] D. O. Scanlon, K. G. Godinho, B. J. Morgan, G. W. Watson, Understanding conductivity anomalies in cu-based delafossite transparent conducting oxides: Theoretical insights, The Journal of Chemical Physics 132 (2) (2010) 024707.

[47] H. Hiramatsu, K. Ueda, H. Ohta, M. Hirano, M. Kikuchi, H. Yanagi, T. Kamiya, H. Hosono, Heavy Hole Doping of Epitaxial Thin Films of a Wide Gap *p*-Type Semiconductor, LaCuOSe, and Analysis of the Effective Mass, Applied Physics Letters 91 (1) (2007) 012104.

[48] K. Ueda, S. Inoue, S. Hirose, H. Kawazoe, H. Hosono, Transparent *p*-Type Semiconductor: LaCuOS Layered Oxysulfide, Applied Physics Letters 77 (17) (2000) 2701.

[49] D. O. Scanlon, J. Buckeridge, C. R. a. Catlow, G. W. Watson, Understanding Doping Anomalies in Degenerate *p*-Type Semiconductor LaCuOSe, Journal of Materials Chemistry C 2 (17) (2014) 3429.

[50] K. Otzschi, H. Ogino, J.-i. Shimoyama, K. Kishio, New Candidates for Superconductors ; A Series of Layered Oxysulfides $(Cu_2S_2)(Sr_{n+1}MnO_{3n-1})$., Journal of Low Temperature Physics 117 (3) (1999) 729–733.

[51] M.-L. Liu, L.-B. Wu, F.-Q. Huang, L.-D. Chen, I.-W. Chen, A promising p-type transparent conducting material: Layered oxysulfide $[cu_2s_2][sr_3sc_2o_5]$, Journal of Applied Physics 102 (11) (2007) 116108.

[52] J. Xu, J.-B. Liu, J. Wang, B.-X. Liu, B. Huang, Prediction of novel p -type transparent conductors in layered double perovskites: A first-principles study, Advanced Functional Materials 28 (26) (2018) 1800332.

[53] G. Hautier, A. Miglio, G. Ceder, G.-M. Rignanese, X. Gonze, Identification and design principles of low hole effective mass p-type transparent conducting oxides., Nature Communications 4 (2013) 2292.

[54] V.-A. Ha, G. Yu, F. Ricci, D. Dahliah, M. J. van Setten, M. Giantomassi, G.-M. Rignanese, G. Hautier, Computationally driven high-throughput identification of CaTe and li3sb as promising candidates for high-mobility p -type transparent conducting materials, Physical Review Materials 3 (3) (2019) 034601.

[55] R. G. Palgrave, P. Borisov, M. S. Dyer, S. R. C. McMitchell, G. R. Darling, J. B. Claridge, M. Batuk, H. Tan, H. Tian, J. Verbeeck, J. Hadermann, M. J. Rosseinsky, Artificial construction of the layered ruddlesden–popper manganite $la_2sr_2mn_3o_{10}$ reflection high energy electron diffraction monitored pulsed laser deposition, Journal of the American Chemical Society 134 (18) (2012) 7700–7714.

[56] J. H. Haeni, C. D. Theis, D. G. Schlom, W. Tian, X. Q. Pan, H. Chang, I. Takeuchi, X.-D. Xiang, Epitaxial Growth of the First Five Members of the $Sr_{n+1}Ti_nO_{3n+1}$ Ruddlesden–Popper Homologous Series, Applied Physics Letters 78 (21) (2001) 3292.

[57] W. Tian, X. Q. Pan, J. H. Haeni, D. G. Schlom, Transmission Electron Microscopy Study of n=1-5 $Sr_{n+1}Ti_nO_{3n+1}$ Epitaxial Thin Films, Journal of Materials Research 16 (07) (2001) 2013–2026.

[58] R. Sayers, N. L. O. Flack, J. Alaria, P. A. Chater, R. G. Palgrave, S. R. C. McMitchell, S. Romani, Q. M. Ramasse, T. J. Pennycook, M. J. Rosseinsky, Epitaxial growth and enhanced conductivity of an IT-SOFC cathode based on a complex perovskite superstructure with six distinct cation sites, Chemical Science 4 (6) (2013) 2403.

[59] I. F. A. e. a. H. Bergerhoff, G. & Brown, Crystallographic databases, Chester, International Union of Crystallography.

[60] W. Sun, S. T. Dacek, S. P. Ong, G. Hautier, A. Jain, W. D. Richards, A. C. Gamst, K. A. Persson, G. Ceder, The thermodynamic scale of inorganic crystalline metastability, Science Advances 2 (11) (2016) e1600225–e1600225.

[61] D. O. Scanlon, A. Walsh, G. W. Watson, Understanding the *p*-Type Conduction Properties of the Transparent Conducting Oxide $CuBO_2$: A Density Functional Theory Analysis, Chemistry of Materials 21 (19) (2009) 4568–4576.

[62] H. T. Evans, The Crystal Structures of Low Chalcocite and Djurleite, Zeitschrift für Kristallographie 150 (1-4) (1979) 299–320.

[63] R. Cava, F. Reidinger, B. Wuensch, Mobile Ion Distribution and Anharmonic Thermal Motion in Fast Ion Conducting Cu_2S, Solid State Ionics 5 (1981) 501–504.

[64] K. Ueda, H. Hosono, Crystal structure of $lacuos_{1-x}se_x$ oxychalcogenides, Thin Solid Films 411 (1) (2002) 115–118.

[65] M. L. Liu, L. B. Wu, F. Q. Huang, L. D. Chen, J. A. Ibers, Syntheses, crystal and electronic structure, and some optical and transport properties of lncuote (ln=la, ce, nd), Journal of Solid State Chemistry 180 (1) (2006) 62–69.

[66] K. Ueda, H. Hosono, N. Hamada, Energy band structure of LaCuOCh (ch = s, se and te) calculated by the full-potential linearized augmented plane-wave method, Journal of Physics: Condensed Matter 16 (28) (2004) 5179–5186.

[67] J. L. Lyons, A. Janotti, C. G. V. de Walle, Effects of carbon on the electrical and optical properties of InN, GaN, and AlN, Physical Review B 89 (3) (2014) 035204.

[68] F. Fuchs, F. Bechstedt, Indium-oxide polymorphs from first principles: Quasiparticle electronic states, Physical Review B 77 (15) (2008) 155107.

[69] K. Parlinski, Z. Q. Li, Y. Kawazoe, First-principles determination of the soft mode in cubic zro_2, Physical Review Letters 78 (21) (1997) 4063–4066.

[70] G. Kresse, J. Furthmüller, J. Hafner, Ab initio force constant approach to phonon dispersion relations of diamond and graphite, Europhysics Letters (EPL) 32 (9) (1995) 729–734.

[71] A. Togo, I. Tanaka, First principles phonon calculations in materials science, Scripta Materialia 108 (2015) 1–5.

[72] E. Pastor, J.-S. Park, L. Steier, S. Kim, M. Grätzel, J. R. Durrant, A. Walsh, A. A. Bakulin, In situ observation of picosecond polaron self-localisation in α-fe$_2$o$_3$ photoelectrochemical cells, Nature Communications 10 (1).

[73] J. Llanos, O. Peña, Electrical resistivity, optical and magnetic properties of the layered oxyselenide SmCuOSe, Journal of Solid State Chemistry 178 (4) (2005) 957–960.

[74] S. J. Clarke, P. Adamson, S. J. C. Herkelrath, O. J. Rutt, D. R. Parker, M. J. Pitcher, C. F. Smura, Structures, Physical Properties, and Chemistry of Layered Oxychalcogenides and Oxypnictides., Inorganic Chemistry 47 (19) (2008) 8473–86.

[75] A. M. Ganose, C. N. Savory, D. O. Scanlon, Beyond methylammonium lead iodide: Prospects for the emergent field of ns^2 containing solar absorbers, Chemical Communications 53 (1) (2017) 20–44.

[76] A. M. Ganose, D. O. Scanlon, Band gap and work function tailoring of sno$_2$ for improved transparent conducting ability in photovoltaics, Journal of Materials Chemistry C 4 (7) (2016) 1467–1475.

[77] A. Walsh, K.-S. Ahn, S. Shet, M. N. Huda, T. G. Deutsch, H. Wang, J. a. Turner, S.-H. Wei, Y. Yan, M. M. Al-Jassim, Ternary Cobalt Spinel Oxides for Solar Driven Hydrogen Production: Theory and Experiment, Energy Environmental Science 2 (7) (2009) 774.

[78] W. Zhu, P. Hor, Crystal structure of new layered oxysulfides: Sr$_3$cu$_2$fe$_2$o$_5$s$_2$ and sr$_2$cumo$_3$s (m=cr, fe, in), Journal of Solid State Chemistry 134 (1) (1997) 128–131.

[79] P. M. Shirage, K. Kihou, C.-H. Lee, H. Kito, H. Eisaki, A. Iyo, Emergence of superconductivity in "32522" structure of (ca$_3$al$_2$o$_5$–y)(fe$_2$pn$_2$) (pn = as and p), Journal of the American Chemical Society 133 (25) (2011) 9630–9633.

[80] H. Hiramatsu, K. Ueda, K. Takafuji, H. Ohta, M. Hirano, T. Kamiya, H. Hosono, Intrinsic Excitonic Photoluminescence and Band-Gap Engineering of Wide-Gap p-Type Oxychalcogenide Epitaxial Films of LnCuOCh (Ln=La, Pr, and Nd: Ch=S or Se) Semiconductor Alloys, Journal of Applied Physics 94 (9) (2003) 5805–5808.

[81] H. Yanagi, S. Park, A. Draeseke, D. Keszler, J. Tate, P-type conductivity in transparent oxides and sulfide fluorides, Journal of Solid State Chemistry 175 (1) (2003) 34–38.

[82] C.-H. Park, D. A. Keszler, H. Yanagi, J. Tate, Gap Modulation in MCu[$Q_{1-x}Q'_x$]F (M=Ba, Sr: Q, Q′=S, Se, Te) and Related Materials, Thin Solid Films 445 (2) (2003) 288–293.

[83] C.-H. Park, R. Kykyneshi, A. Yokochi, J. Tate, D. A. Keszler, Structure and physical properties of BaCuTeF, Journal of Solid State Chemistry 180 (5) (2007) 1672–1677.

[84] W. J. Zhu, P. H. Hor, Sr_2cugao_3s, a rare example of square pyramidal gallium, Inorganic Chemistry 36 (17) (1997) 3576–3577.

[85] J. S. O. Evans, E. B. Brogden, A. L. Thompson, R. L. Cordiner, Synthesis and characterisation of the new oxyselenide $bi_2yo_4cu_2se_2$, Chemical Communications (8) (2002) 912–913.

[86] W. Zhu, P. Hor, Unusual layered transition-metal oxysulfides: $Sr_2cu_2mo_2s_2$ (m=mn, zn), Journal of Solid State Chemistry 130 (2) (1997) 319–321.

[87] H. Hirose, K. Ueda, H. Kawazoe, H. Hosono, Electronic structure of $sr_2cu_2zno_2s_2$ layered oxysulfide with cus layers, Chemistry of Materials 14 (3) (2002) 1037–1041.

[88] G. Kresse, J. Hafner, *Ab-initio* molecular dynamics for liquid metals, Physical Review B 47 (1) (1993) 558–561.

[89] G. Kresse, J. Hafner, *Ab-initio* molecular-dynamics simulation of the liquid-metal amorphous-semiconductor transition in germanium, Physical Review B 49 (20) (1994) 14251–14269.

[90] G. Kresse, J. Furthmüller, Efficient Iterative Schemes for *Ab-Initio* Total-Energy Calculations Using a Plane-Wave Basis Set., Physical Review B 54 (16) (1996) 11169–11186.

[91] G. Kresse, J. Furthmüller, Efficiency of *Ab-initio* total energy calculations for metals and semiconductors using a plane-wave basis set, Computational Materials Science 6 (1) (1996) 15–50.

[92] J. P. Perdew, A. Ruzsinszky, G. I. Csonka, O. A. Vydrov, G. E. Scuseria, L. A. Constantin, X. Zhou, K. Burke, Restoring the density-gradient expansion for exchange in solids and surfaces, Physical Review Letters 100 (13) (2008) 136406.

[93] P. Blochl, Projector Augmented-Wave Method, Physical Review B 50 (24) (1994) 17953–17979.

[94] P. Pulay, Ab initio calculation of force constants and equilibrium geometries in polyatomic molecules. I. Theory (Reprinted from Molecular Physics, vol 17, pg 197-204, 1969), Molecular Physics 100 (1) (2002) 57–62.

[95] J. Buckeridge, D. O. Scanlon, A. Walsh, C. R. A. Catlow, Automated Procedure to Determine the Thermodynamic Stability of a Material and the Range of Chemical Potentials Necessary for its Formation Relative to Competing Phases and Compounds, Computational Physics Communication 185 (1) (2014) 330–338.

[96] A. V. Krukau, O. a. Vydrov, A. F. Izmaylov, G. E. Scuseria, Influence of the exchange screening parameter on the performance of screened hybrid functionals, Journal of Chemical Physics 125 (22) (2006) 224106.

[97] B. Adolph, J. Furthmüller, F. Bechstedt, Optical properties of semiconductors using projector-augmented waves, Physical Review B 63 (12) (2001) 125108.

[98] G. K. Madsen, D. J. Singh, BoltzTraP. a code for calculating bandstructure dependent quantities, Computer Physics Communications 175 (1) (2006) 67–71.

[99] H. Fröhlich, Electrons in lattice fields, Advances in Physics 3 (11) (1954) 325–361.

[100] D. Davies, C. Savory, J. M. Frost, D. Scanlon, B. Morgan, A. Walsh, Descriptors for Electron and Hole Charge Carriers in Metal Oxides, ChemRxiv (DOI: 10.26434/chemrxiv.11214914.v1).

[101] A. M. Ganose, A. J. Jackson, D. O. Scanlon, sumo: Command-line tools for plotting and analysis of periodic ab-initio calculations, Journal of Open Source Software 3 (28) (2018) 717.

[102] B. H. Toby, EXPGUI, a graphical user interface for GSAS, Journal of Applied Crystallography 34 (2) (2001) 210–213.

[103] P. Kubelka, New contributions to the optics of intensely light-scattering materials part i, Journal of the Optical Society of America 38 (5) (1948) 448.

[104] J. Tauc, R. Grigorovici, A. Vancu, Optical properties and electronic structure of amorphous germanium, physica status solidi (b) 15 (2) (1966) 627–637.

[105] J. Tauc, Optical properties and electronic structure of amorphous ge and si, Materials Research Bulletin 3 (1) (1968) 37–46.

Figures

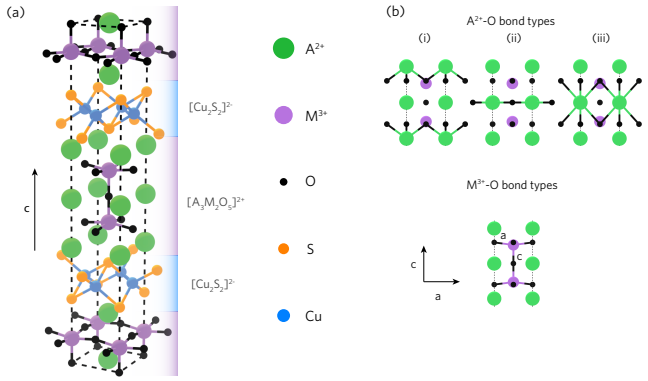

Figure 1: The $[Cu_2S_2][Sr_3Sc_2O_5]$ (a) and the crystal structure as viewed along the [100] direction where Cu=blue, S=orange, A^{2+}=green, M^{3+}=purple and O=black. (b) shows the different bond types for A^{2+}–O and M^{3+}–O.

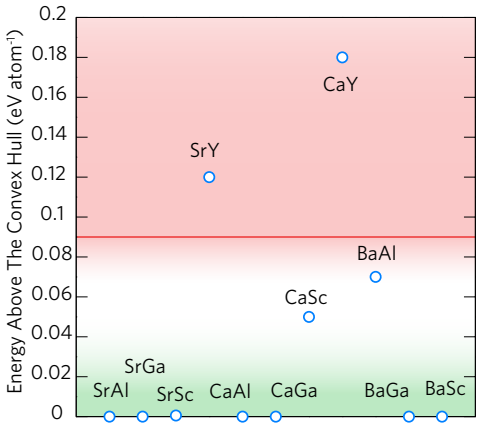

Figure 2: A depiction of the stable and metastable compounds with respect to the stability criterion 0–0.09 eV atom^{-1}. The green area is the predicted "stable" region (0–0.02 eV atom^{-1}), the white region depicts the area of metastability (0.02–0.09 eV atom^{-1}) and the red region the unstable region (> 0.09 eV atom^{-1}). The graph predicts nine potentially stable variations on the $[Cu_2S_2][Sr_3Sc_2O_5]$ structure.

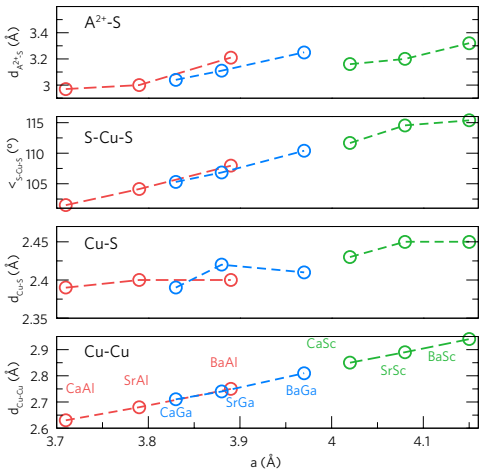

Figure 3: The bond lengths and angles related to the valence band ($[Cu_2S_2]^{2-}$ layer), Cu–Cu, Cu–S, S–Cu–S and A^{2+}–S with respect to increasing basal lattice parameter.

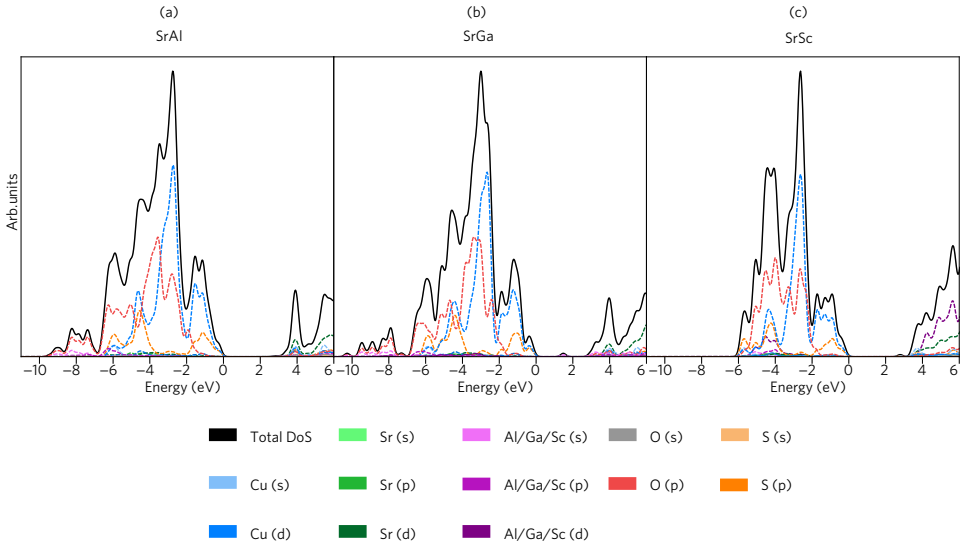

Figure 4: Representative density of states (DOS) for the different groups, SrAl, SrGa and the parent compound: SrSc. In each example the valence band maximum is set to 0 eV. Full partial and total DOS for all other compounds can be found in SI Figure S1.

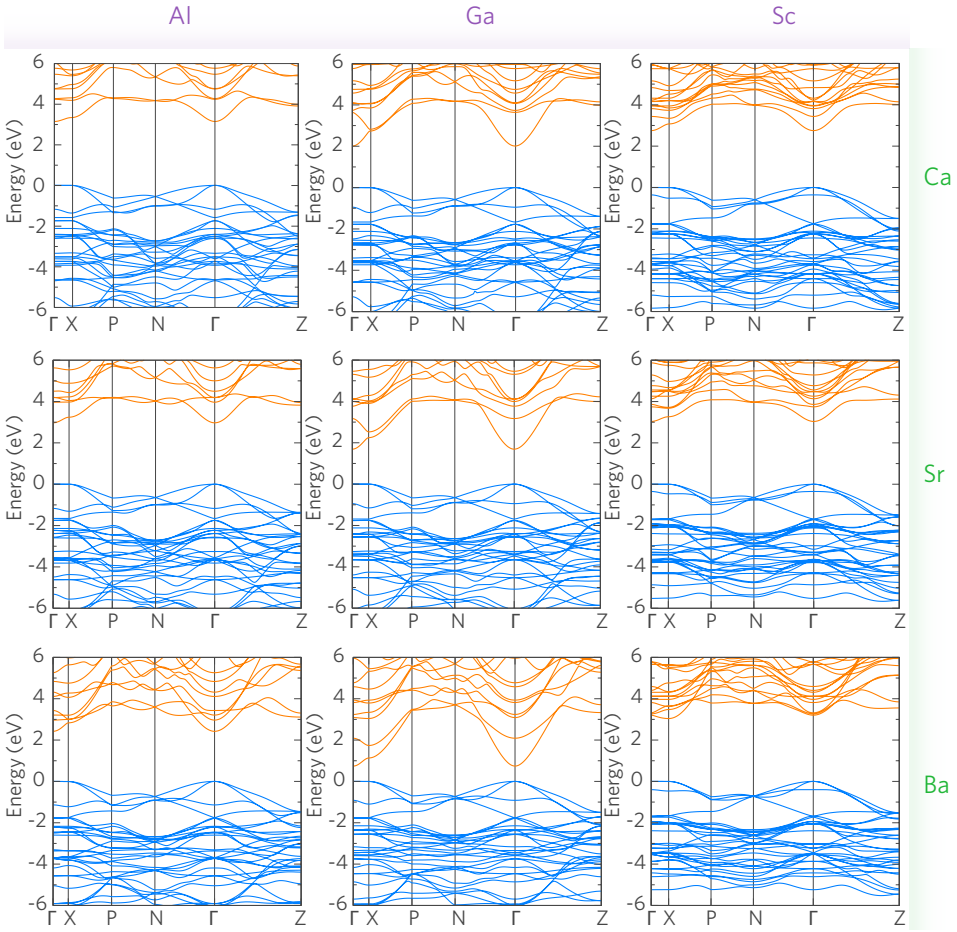

Figure 5: The combined band structures for the stable and metastable $[Cu_2S_2][A_3M_2O_5]$ compounds calculated using the HSE06 functional. The band structures are arrayed in a grid such that the top left corresponds to CaAl and the bottom right to BaSc. In the stable examples, the valence bands are depicted in blue and the conduction bands in orange, where the VBM is set to 0 eV. The band structures are ordered in terms of increasing A^{2+} cation ionic radii (Ca → Sr → Ba) and in terms of increasing M^{3+} cation radii(Al → Ga → Sc).

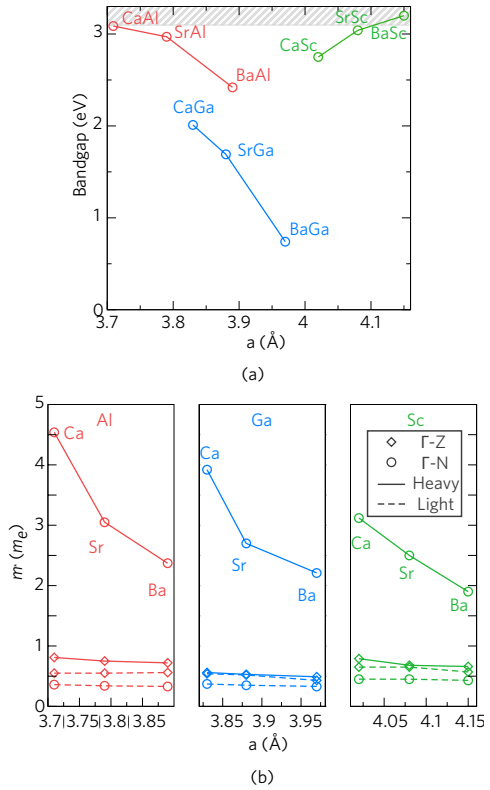

Figure 6: (a) The direct fundamental band gap as a function of increasing a parameter. The hashed grey region corresponds to the visible light transparency region. (b) The VBM hole effective mass as a function of increasing a parameter.

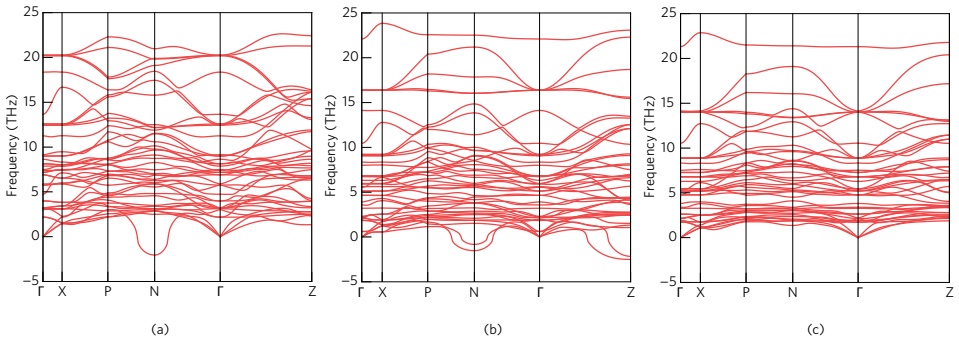

Figure 7: The phonon dispersion for (a) CaAl, (b) SrSc, (c) BaSc. SrSc and BaSc are both in the *I4/mmm* whilst CaAl is in the *C2/m* space group.

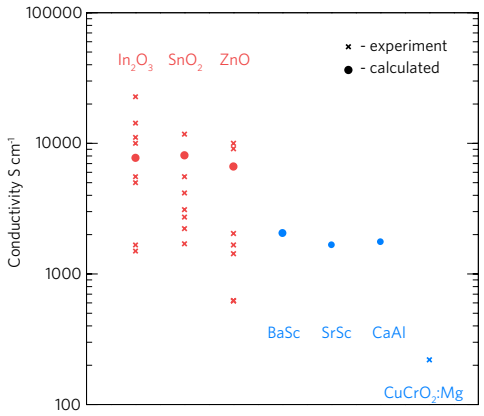

Figure 8: The calculated and experimental conductivities for n-type TCs (In_2O_3,SnO_2,ZnO) shown in red and the *p*-type transparent conductors shown in blue. $CuCrO_2$:Mg refers to Mg-doped $CuCrO_2$. The values are taken for a doping level of $\sim 1 \times 10^{21}$ cm^{-3}. References are included in SI Table S6

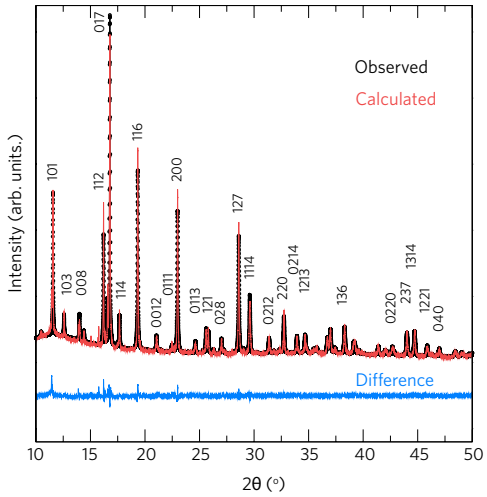

Figure 9: Indexed synchotron powder x-ray diffraction pattern collected using the I11 beamline at the Diamond Light Source, with a wavelength of 0.82603 Å. Black crosses represent the observed diffraction data; the red line, the calculated diffraction pattern and blue line, the difference between these values. This plot shows the final Rietveld refinement model of $[Cu_2S_2][Ba_3Sc_2O_5]$. Note that different scales are used on the intensity and difference plots. The peak at $\sim 11.44°$ arises from diluting emulsion added to the sample to reduce x-ray absorption.

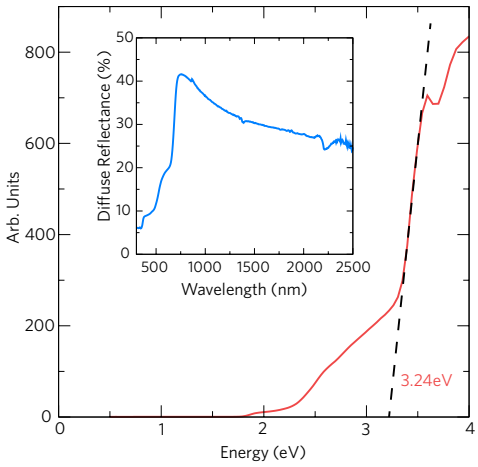

Figure 10: Tauc plot, $[f(R)h\nu]^2$ vs. photon energy, derived from the raw diffuse reflectance spectrum (inset) collected over a range of 300–2500 nm at intervals of 5 nm. The dashed line extrapolated to the abscissa models the linear region of absorption edge for calculation of the band gap energy.

Tables

Table 1: The structural parameters and bond lengths for all stable predicted compounds calculated using HSE06. The compounds are ordered in groups relating to M^{3+} and within these groups in terms of increasing cell lattice parameter (a)(any experimental results are shown in italics). The different A^{2+}–O and M^{3+}–O bond types are shown in Figure 1 and the S–Cu–S bond angles refer to "in-plane" bond angles.

Compound	a /Å	c /Å	vol /Å^3	$d_{Cu–Cu}$ /Å	$d_{Cu–S}$ /Å	$<_{S–Cu–S}$ /°	$d_{M^{3+}–O}$ (c, a) /Å	$d_{A^{2+}–O}$ (i,ii,iii)/Å	$d_{A^{2+}–S}$ /Å
CaAl	3.71	25.66	353.84	2.63	2.39	101.50	1.78, 1.88	2.36, 2.63, 2.78	2.97
SrAl	3.79	26.77	384.47	2.68	2.40	104.13	1.78, 1.92	2.51, 2.68, 2.82	3.00
BaAl	3.89	28.26	427.34	2.75	2.41	107.95	1.80, 1.97	2.69, 2.75, 2.89	3.21
CaGa	3.83	25.66	376.07	2.71	2.39	105.30	1.87, 1.93	2.37, 2.71, 2.90	3.04
SrGa	3.88	26.72	401.88	2.74	2.42	106.85	1.87, 1.96	2.53, 2.74, 2.91	3.11
BaGa	3.97	28.22	445.08	2.81	2.41	110.40	1.91, 2.01	2.70, 2.81, 2.99	3.25
CaSc	4.02	25.25	407.69	2.85	2.43	111.67	1.98, 2.03	2.41, 2.84, 3.01	3.16
SrSc	4.08	26.07	433.45	2.89	2.45	114.55	1.97, 2.05	2.55, 2.88, 3.04	3.20
SrSc[50]	*4.08*	*25.99*	*433.45*	*2.88*	*2.49*	*110.00*	*1.91,2.07*	*2.51,2.88,3.05*	*3.18*
BaSc	4.15	27.44	472.11	2.94	2.45	115.37	1.99, 2.09	2.70, 2.93, 3.07	3.32

Table 2: The percentage of states at the VBM in the thermodynamically stable $[Cu_2S_2][A_3M_2O_5]$ compounds together with the width of the valence band. Significant contributions are indicated in bold. The total DOS and partial DOS is displayed in SI Figure S1.

Compound	Cu:s,p,d /%	S:s,p,d /%	A^{2+}:s,p,d/%	M^{3+}:s,p,d /%	O:s,p,d /%	VB width /eV
CaAl	0,1,**49**	0,**45**,0	0,2,2	0,0,0	0,1,0	9.5
SrAl	0,1,**51**	0,**45**,0	0,1,1	0,0,0	0,1,0	9.2
BaAl	0,1,**52**	0,**43**,0	0,1,1	0,0,0	0,1,0	9.2
CaGa	0,1,**52**	0,**44**,0	0,2,2	0,0,0	0,1,0	10.3
SrGa	0,1,**53**	0,**44**,0	0,1,1	0,0,0	0,1,0	10.0
BaGa	0,1,**53**	0,**42**,0	0,1,1	0,0,0	0,1,0	9.9
CaSc	0,1,**55**	0,**41**,0	0,1,1	0,0,0	0,1,0	5.9
SrSc	0,2,**55**	0,**41**,0	0,1,1	0,0,0	0,2,0	5.5
BaSc	0,2,**55**	0,**41**,0	0,1,1	0,0,0	0,1,0	5.4

Table 3: The percentage of states at the CBM in the thermodynamically stable $[Cu_2S_2][A_3M_2O_5]$ compounds. Significant contributions are indicated in bold. The total DOS and partial DOS is displayed in SI Figure S1.

Compound	Cu:s,p,d /%	S:s,p,d /%	A^{2+}:s,p,d/%	M^{3+}:s,p,d /%	O:s,p,d /%
CaAl	**20**,0,0	**28**,10,0	**22**,4,0	5,1,0	8,2,0
SrAl	**22**,0,1	**29**,5,0	8,2,1	**14**,2,0	**13**,5,0
BaAl	**11**,0,2	**14**,0,0	8,0,9	**30**,3,0	**17**,6,0
CaGa	8,0,1	**11**,0,0	7,1,0	**51**,3,1	**17**,0,0
SrGa	6,0,1	8,0,0	2,0,1	**56**,2,0	**23**,0,0
BaGa	2,0,1	2,0,0	1,0,1	**68**,4,0	**16**,0,0
CaSc	**20**,0,1	**32,11**,0	**18**,1,1	2,0,3	9,0,0
SrSc	**24**,0,1	**33,13**,0	**13**,3,0	3,0,3	6,2,0
BaSc	**34**,0,15	0,0,0	0,0,**47**	0,0,0	2,1,0

Table 4: The fundamental direct and indirect band gaps together with the optical band gap for the $[Cu_2S_2][A_3M_2O_5]$ compounds alongside the various effective masses for both the VBM and CBM. The optical gap value is taken from α^2 as seen in SI Figure S3. The direct gaps for BaSc are displayed for the direct transition at X and the direct transition at Γ.

Compound	E_g^{fund}/eV	E_g^{opt}/eV	$m^*_{[\Gamma-X]}$ / m_e		$m^*_{[\Gamma-N]}$/ m_e			$m^*_{[\Gamma-Z]}$/ m_e			
				VBM	CBM	VBM (h)	VBM (l)	CBM	VBM (h)	VBM (l)	CBM
CaAl	3.14	-	3.17	*85.30*	0.52	4.54	0.37	0.36	0.81	0.55	0.31
SrAl	2.97	-	3.00	*44.98*	0.39	3.05	0.36	0.34	0.75	0.55	0.34
BaAl	2.42	-	2.46	*17.34*	0.32	2.37	0.37	0.33	0.72	0.56	0.33
CaGa	2.01	-	2.03	*85.31*	0.23	3.92	0.37	0.25	0.70	0.61	0.26
SrGa	1.69	-	1.71	*45.14*	0.24	2.70	0.35	0.23	0.62	0.59	0.23
BaGa	0.74	-	0.78	*31.30*	0.25	2.21	0.33	0.20	0.60	0.52	0.20
CaSc	2.75	-	2.78	*22.16*	0.37	3.12	0.45	0.34	0.77	0.76	0.33
SrSc	3.04	-	3.06	*47.42*	0.45	2.50	0.45	0.35	0.75	0.73	0.35
BaSc	3.24	3.04 (Γ–X)	3.24	*28.54*	0.95 (X–Γ)	1.90	0.43	0.35 (X–P)	0.72	0.63	-

Table 5: The structural parameters, bond lengths and optical band gap for the BaSc powders.

Parameters	Experiment	HSE06
a /Å	4.14	4.15
c /Å	27.12	27.44
$d_{Cu–Cu}$ /Å	2.93	2.94
$d_{Cu–S}$ /Å	2.44	2.45
$<_{S–Cu–S}$ /°	116.07	115.37
$d_{M^{3+}–O}$ (c, a) /Å	2.00,2.08	1.99,2.09
$d_{A^{2+}–O}$ (i,ii,iii) /Å	2.71,2.93,3.04	2.70,2.93,3.07
$d_{A^{2+}–S}$ /Å	3.30	3.32
E_g^{opt} /eV	3.24	3.24